White Rose Research Online
eprints@whiterose.ac.uk
https://eprints.whiterose.ac.uk
Universities of Leeds, Sheffield and York

Deposited via The University of Sheffield.

White Rose Research Online URL for this paper:
https://eprints.whiterose.ac.uk/id/eprint/185354/

Version: Accepted Version

Article:

Zhou, L., Bai, W., Han, Z. et al. (2022) Comparison of the damage and microstructure evolution of eutectoid and hypereutectoid rail steels under a rolling-sliding contact. Wear, 492-493. 204233. ISSN: 0043-1648

https://doi.org/10.1016/j.wear.2021.204233

© 2022 Elsevier B.V. This is an author produced version of a paper subsequently published in Wear. Uploaded in accordance with the publisher's self-archiving policy. Article available under the terms of the CC-BY-NC-ND licence (https://creativecommons.org/licenses/by-nc-nd/4.0/).

Reuse
This article is distributed under the terms of the Creative Commons Attribution-NonCommercial-NoDerivs (CC BY-NC-ND) licence. This licence only allows you to download this work and share it with others as long as you credit the authors, but you can’t change the article in any way or use it commercially. More information and the full terms of the licence here: https://creativecommons.org/licenses/

Takedown
If you consider content in White Rose Research Online to be in breach of UK law, please notify us by emailing eprints@whiterose.ac.uk including the URL of the record and the reason for the withdrawal request.

UNIVERSITY OF LEEDS
University of Sheffield
UNIVERSITY of York

Comparison of the damage and microstructure evolution of eutectoid and hypereutectoid rail steels under a rolling-sliding contact

L. Zhou[a], W. Bai[a,b], Z.Y. Han[a,b], W.J. Wang[a], Y. Hu[a], H.H. Ding[a*], R. Lewis[c], E. Meli[d], Q.Y. Liu[a], J. Guo[a]

[a] *Tribology Research Institute, State Key Laboratory of Traction Power, Southwest Jiaotong University, Chengdu 610031, China*

[b] *Pangang Group Panzhihua Iron and steel Research Institute Co. Ltd, Panzhihua 617000, China*

[c] *Department of Mechanical Engineering, The University of Sheffield, Mappin Street, Sheffield, S1 3JD, UK*

[d] *Department of Industrial Engineering, University of Florence, Firenze 50139, Italy*

Abstract: The wear and rolling contact fatigue (RCF) performance of eutectoid and hypereutectoid rail steels were studied. Subsequently, the microstructure evolutions of subsurface materials of these two rail steels after testing were comparatively investigated. The results indicated that, compared with the eutectoid rail, the hypereutectoid rail had lower wear loss, but longer RCF crack lengths. After the rolling-sliding testing, the original equiaxed and undeformed coarse grains of rails in the matrix were transformed into nano-grains rich in high angle grain boundaries (HAGBs). The microstructure evolution of rail steels under rolling-sliding contact could be result from two mechanisms. Firstly, the initial deformation and the breaking of the lamellar structure of pearlite grains occurs through the movement of dislocations. Secondly, the formation of the nanostructure grains happens through continuous dynamic recrystallization (cDRX). Compared with the eutectoid rail, the hypereutectoid rail had finer interlamellar spacing and higher contents of low angle grain boundaries (LAGBs) in the matrix. After the rolling-sliding testing, the hypereutectoid rail had more severe LAGBs-to-HAGBs transitions and and a more severe cDRX process than the eutectoid rail, which might be

---

[*] Corresponding author. Tel: +86-28-87634304.

E-mail address: haohao.ding@swjtu.edu.cn (H.H. Ding).

the reason for the longer RCF crack lengths it exhibited.

Keywords: Hypereutectoid rail; RCF; Plastic deformation; Rolling-sliding contact; Microstructure evolution

1. Introduction

Wear and rolling contact fatigue (RCF) damage can be widely found on rails in the field. They can significantly shorten the service life of rail [1]. Due to the complex working conditions, the wear and damage of rail material is varied, such as side wear, corrugation, squats, oblique cracks and scratches [2-5]. Various methods have been introduced to prevent the damages of rails [6-8]. However, the most effective way of reducing damage and minimise the maintenance costs is through developing advanced high strength steels [8].

The microstructure parameters of the original pearlite grains, such as the interlamellar spacing, the pearlite nodule size and the pre-austenite size, are the main factors that determine the mechanical properties [9] and wear and damage behaviour [10] of pearlitic rail materials. The decrease in the diameter of pearlite nodule and the interlamellar spacing could enhance the grain refinement and improve the wear resistance of rail materials [11]. Furthermore, the refinement in the interlamellar spacing could also decrease the crack propagation rate in pearlite [12]. Therefore, the development of higher strength and finer pearlitic structure rail steel would be the main task in the manufacturing of rails [13,14]. Due to their high hardness and wear resistance, hypereutectoid steels (e.g., C wt%>0.77%) were introduced into railway lines. These had an extremely fine interlamellar spacing and nearly no second cementite in the matrix. As reported in the literature [8,12,14,15], the hypereutectoid rails had obvious advantages in wear and RCF resistances and could be a potential heavy haul railway steel.

Subjected to the thermo and the mechanical loads, various microstructure transitions can be found in the subsurface of pearlitic rail, which could significantly influence the RCF damage behaviour of rail. Under normal and tangential forces, the originally randomly distributed pearlite is rearranged to the running direction, which leads to the anisotropy in the mechanical properties of the rail surface material [16]. Masoumi et al. [17] found that the {110} texture could accelerate crack propagation while the {111} texture inhibits the crack propagation in pearlitic rail. The surface material of rail experiences large shear plastic deformation and grain refinement. The accumulated shear strain on the rail top surface can reach 1300% to 1900% [18,19], and the grain size can be refined into diameters of around 1 μm [20]. White etching layers (WELs) with high hardness and low fracture toughness can usually also be observed on heavily loaded and curved railway line [2]. Kumar et al. [21] found that the pearlite is transformed into martensite and austenite in WEL as a result of high temperature and severe plastic deformation. Another microstructure transition in pearlitic rail steel is the decomposition of cementite and the resulting solid solution strengthening [22,23]. The cementite's dissolution could be realized through the dislocations dragging the C atoms form cementite to ferrite because the binding energy between the C atoms and dislocations (0.75 eV) iss larger than that in cementite (0.40-0.42 eV) [24]. Furthermore, the cementite dissolution could also be realized through severe plastic deformation, as evidenced by high pressure torsion [25] and cold drawing [26] processes.

Under the cyclic loading, the rail material accumulates elastic and plastic deformation until reaching a ratchetting limit (i.e., ratcheting failure) [16,27]. According to the theory of delamination wear [28], the plastic deformation and the strain hardening accumulate gradually from the matrix to the worn surface, eventually resulting in surface defects, fatigue cracks and the material removal. When the surface material is removed by wear, the subsurface material becomes the new surface material and participates in the wear and damage processes. Therefore, the microstructure evolution of the subsurface materials directly influences the wear and RCF behaviour of rail materials. However, it is difficult to analyze the failure process of the surface material after different numbers of cycles. While, studying the microstructure evolutions of different regions along the depth could reveal the plastic deformation and defect accumulation processes of rail.

As mentioned above, except for the original microstructure, the study on the shear deformation induced microstructure modification of rail material is crucial for understanding the failure mechanism of rail. Microstructure evolution of rail steel is a multi-scale processes from the microscale (i.e., grain refinement) to atomic scale (i.e., cementite decomposition). Therefore, advanced characterization methods are necessary for its study. In the present investigation, rolling-sliding tests were performed on the JD-1 wheel-rail simulation test rig. Then, the microstructure evolution of the subsurface material between eutectoid and hypereutectoid rail steels at different depths was comparatively investigated via scanning electron microscopy (SEM), electron backscattered diffraction (EBSD) and transmission electron microscopy (TEM).

2. Experimental details

2.1 Experimental materials and parameters

In the present study, two types of rail steel were selected: eutectoid rail and hypereutectoid rail, both of which are applied in heavy haul railway lines in China. The microstructure of the as-received rail material is presented in Fig. 1a and b. Both the eutectoid and the hypereutectoid rail steels had a pearlite structure that contained alternative cementite and ferrite plates. Through the circular line counting method [29], the average values of pearlite lamellar spacing of the eutectoid and hypereutectoid steels was found to be 136 nm and 97 nm, respectively. Table 1 shows the chemical compositions and hardness of the rail steels. The hypereutectoid rail had a higher carbon content (0.90~0.95 wt%) and higher hardness (405$HV_{0.5}$) than the eutectoid rail (0.71~0.80 wt% and 355 $HV_{0.5}$).

The rolling-sliding wear tests were performed on the JD-1 wheel-rail simulation test rig. A detail description of the JD-1 test rig can be found in a previous study [30]. The rolling-sliding contact and dimensions of the simulated wheel and rail rollers in the present study are shown in Fig. 2. The wheel roller had a cylindrical shape with a diameter of 1050 mm. The tested rail rollers were cut from the railhead with an ellipsoid shape. The diameter of the rail rollers in the rolling direction was 62 mm and 61 mm in the transverse direction. The normal force between the wheel roller and the rail roller was 3100 N, leading to a maximum contact pressure of 1729 MPa at the contact region according to the Hertzian simulation theory. A tangential force of approximately 390 N was applied on the rail roller. The rotational speed of the rail roller was 508 rpm. The number of cycles for the rail rollers was set at 10^6. Each test was carried out at least twice.

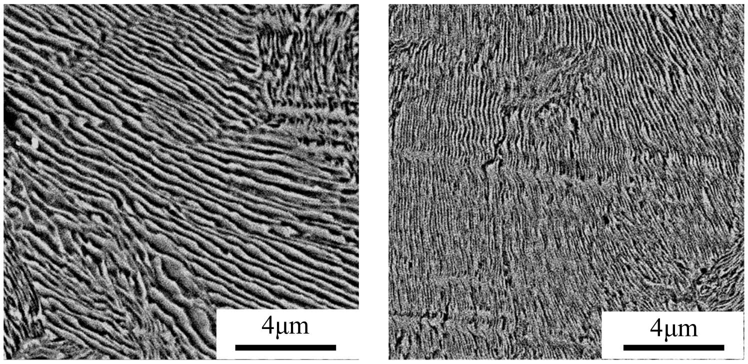

(a) (b)

Fig. 1. Original microstructures of rail steels, (a) eutectoid rail; (b) hypereutectoid rail.

Table 1 Chemical compositions of rail steels (wt %) and hardness ($HV_{0.5}$).

Rail	C	Mn	Si	Cr	P	S	Hardness
Eutectoid	0.71~0.80	0.50~0.70	0.70~1.05	≤0.20	≤0.03	≤0.03	355±8
Hypereutectoid	0.90~0.95	0.94~1.02	0.48~0.52	0.22~0.23	0.01~0 .014	0.04~0.07	405±10

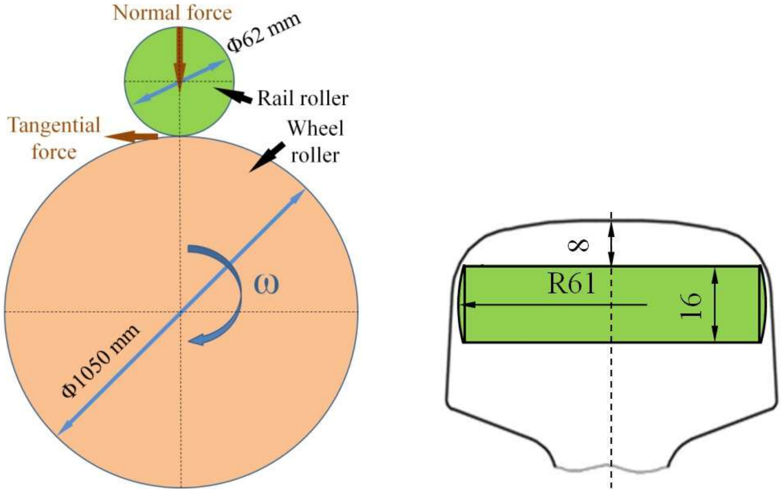

(a) (b)

Fig. 2. (a) Illustration of the rolling-sliding contact of wheel-rail rollers and (b) sampling position and dimensions of rail rollers.

2.2 Microstructure characterization

Before and after the rolling-sliding tests, the rail rollers were ultrasonically cleaned in ethyl. Then the mass of the rollers was measured using an electronic balance (JA4103, China, accuracy: 0.0001g). To characterise the work hardening of rail after a test, a Vickers hardness tester (MVK-H21, Japan) was utilized. To observe the plastic deformation and subsurface cracks of rail materials after testing, samples that ran parallel to the running direction were prepared for optical microscope (OM) (KEYENCE VHX-6000, Japan) and scanning electron microscopy (SEM) (JSM 7800F, Japan) observation.

The samples for EBSD analysis were taken from the rail material by wire cutting along the running direction. Three different tested zones were selected for EBSD observation in the present study: the severely deformed zone in the outermost layer (near the worn surface), the transition zone (30 μm from the worn surface), and the matrix zone (1mm from the worn surface where almost none plastic deformation could be observed). After being mechanically ground and polished, the samples were electropolished in a solution that contained 12 ml distilled water and 80 ml alcohol and 8ml perchloric acid at a voltage of 16V for 30s. EBSD analysis was conducted on a SEM (Hitachi S-3400N, Japan) equipped with HKL-EBSD probe and HKL Channel 5 system. The working parameters for EBSD observation are described as follows: the accelerating voltage was 20 kV, the emission current was 80 μA and the working distance was 14~17 mm. The samples were inclined 70° with respect to the incident electron. The scanning step size was defined as 0.075 μm, 0.3 μm and 0.6 μm in the severe deformed zone, transition zone and matrix zone, respectively.

Microstructure observation of the subsurface material of eutectoid and hypereutectoid rail steels after testing was also carried out on a transmission electron microscope (TEM) (Hitachi H-800, the USA) selected area electron diffraction (SAED) and bright field (BF) TEM. The sample preparation method is described as follows. First, a wire cutting machine was used to cut samples along the running direction from the rail material. Then samples were mechanically ground and polished. Finally, focused ion beam (FIB) was used to take samples from the severe deformed zone and the transition zone for observation. The samples in the severely deformed zone were taken as close to the surface as possible, while samples in the transition zone were taken from a distance of 50 μm from the worn surface.

3. Results and discussion

3.1 Wear and RCF cracks

Fig. 3a shows the mass losses and surface hardness of eutectoid and hypereutectoid rail steels after testing. It could be observed that the hypereutectoid rail steel with higher hardness has lower mass loss and lower surface hardness after testing than eutectoid rail. Therefore, the hypereutectoid rail has better resistance to wear and work hardening than eutectoid rail. Fig. 3b shows the RCF crack daa for eutectoid and hypereutectoid rail steels. It could be observed that the hypereutectoid rail has longer crack lengths, but a shallower crack depth than eutectoid rail.

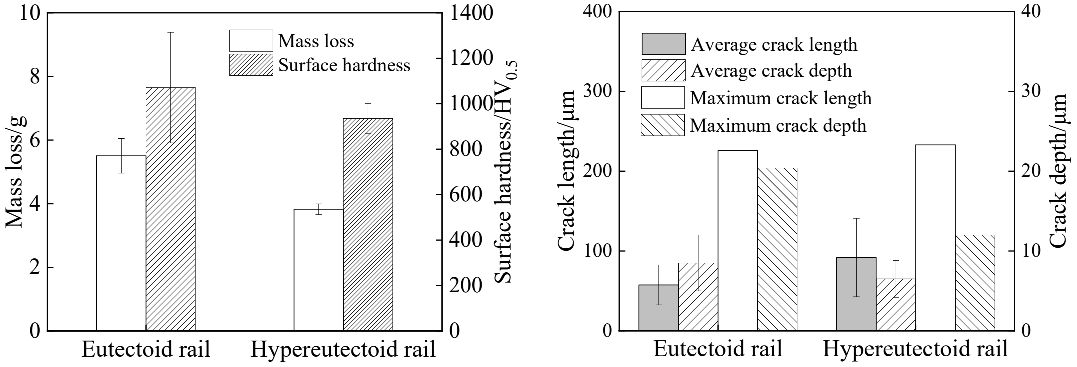

(a) (b)

Fig. 3. (a) Mass losses and surface hardness; (b) statistical RCF cracks of eutectoid and hypereutectoid steels after testing.

3.2 Sectional OM and SEM observation

The overall morphology of plastic deformation of eutectoid and hypereutectoid rails was observed through OM, as shown in Fig. 4. The plastic deformation depth of eutectoid rail is 73 μm, which is larger than that of hypereutectoid rail (64 μm). Furthermore, the topmost materials both of eutectoid and hypereutectoid rails have been refined and could not be identified under OM.

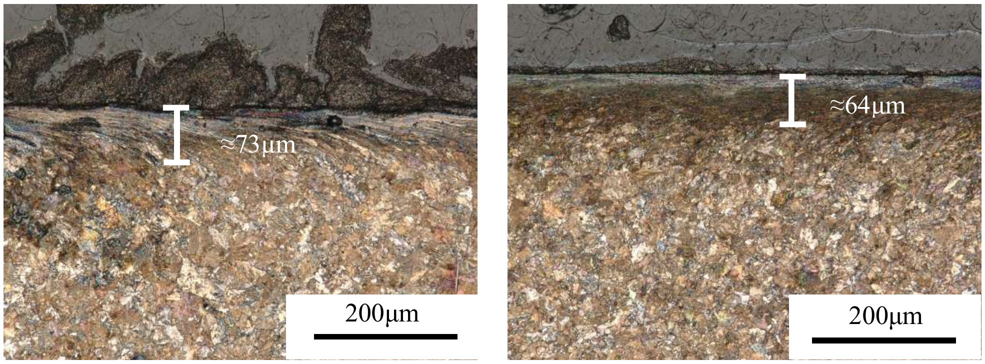

(a) (b)

Fig. 4. OM observation of the plastic deformation of rails, (a) eutectoid rail and (b) hypereutectoid rail.

The microstructure of the subsurface materials of eutectoid and hypereutectoid rail steels after testing were observed via SEM, as shown in Fig. 5. With increasing distance from the worn surface, the plastic deformation and the material defects alleviate gradually until reaching the bulk matrix. According to the degree of plastic deformation, the subsurface material after testing could be divided into three zones: the severly deformed zone (within 30 μm from the worn surface), the transition zone (within 30-70μm from the worn surface) and the matrix zone.

In the present study, both the eutectoid and hypereutectoid rail steels contain alternating ferrite and cementite plates (Fig. 1). Due to the higher content of slip systems, the ferrites plates deform much more easily than cementite under the action of the shear force [23]. Therefore, the morphologies of cementite could reflect the microstructure deformation of the pearlite grains. It could be observed that, in the transition zone (the initial stage of deformation) (Fig. 5a and c), the deformation behaviour of cementite and material defects are highly dependent on the orientation of pearlite lamellar in the rolling direction (RD). When the orientation of the initial pearlite lamellar is consistent with the RD, the material defects are dominated by the shortening of the pearlite lamellar spacing and the curled cementite. When the initial pearlite lamellar is arranged perpendicular or at a large angle to the RD, the material defects are dominated by cementite twisting and breaking. In the severely deformed zone (Fig. 5b and d), the cementite plates are thinned and broken into granules. A fibrous structure that is nearly parallel to the RD could also be observed.

As for the eutectoid rail, both the curled and broken cementite could be observed in the transition zone (Fig. 5a). However, due to the smaller interlamellar spacing, the material defects are dominated by curled cementite in the hypereutectoid rail (Fig. 5c). In summary, the cementite plates in the hypereutectoid rail have better resistance to deformation and breakage than those in the eutectoid rail.

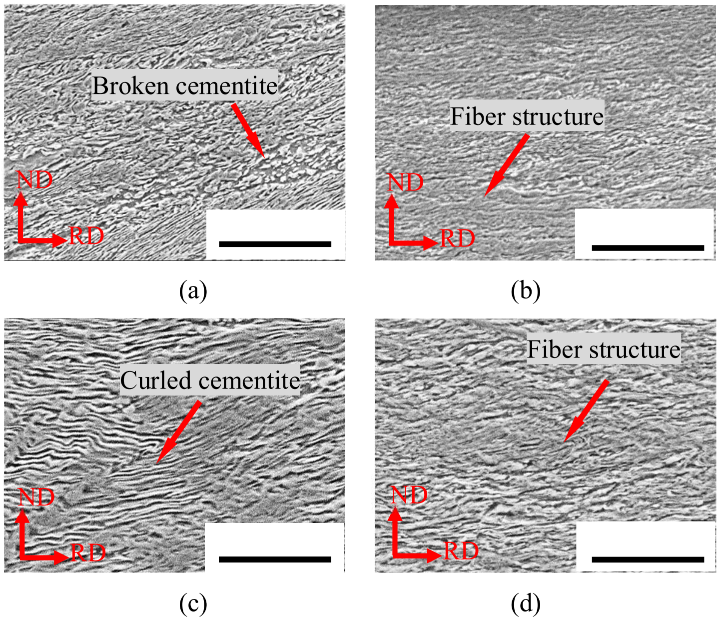

(a) (b)

(c) (d)

Fig. 5. SEM observation of microstructure deformation of rail, (a) eutectoid rail-transition zone; (b) eutectoid rail-severe deformed zone; (c) hypereutectoid rail-transition zone; (d) hypereutectoid rail-severe deformed zone.

3.3 EBSD observation

Fig. 6 shows the inverse pole figures (IPFs) of eutectoid and hypereutectoid rail steels in different zones after testing. The color in the IPF maps represents the grain orientation that is parallel to the reference direction (the rolling direction). It can be observed that the grain orientation both of eutectoid and hypereutectoid rail are randomly distributed in the matrix zone

(Fig. 6a and d). In the transition zone, grains with {111} orientation in hypereutectoid rail (Fig. 6e) is the dominant preferred orientation in the RD plane. In the severely deformed zone, the grains of rails orientate randomly again (Fig. 6c and f).

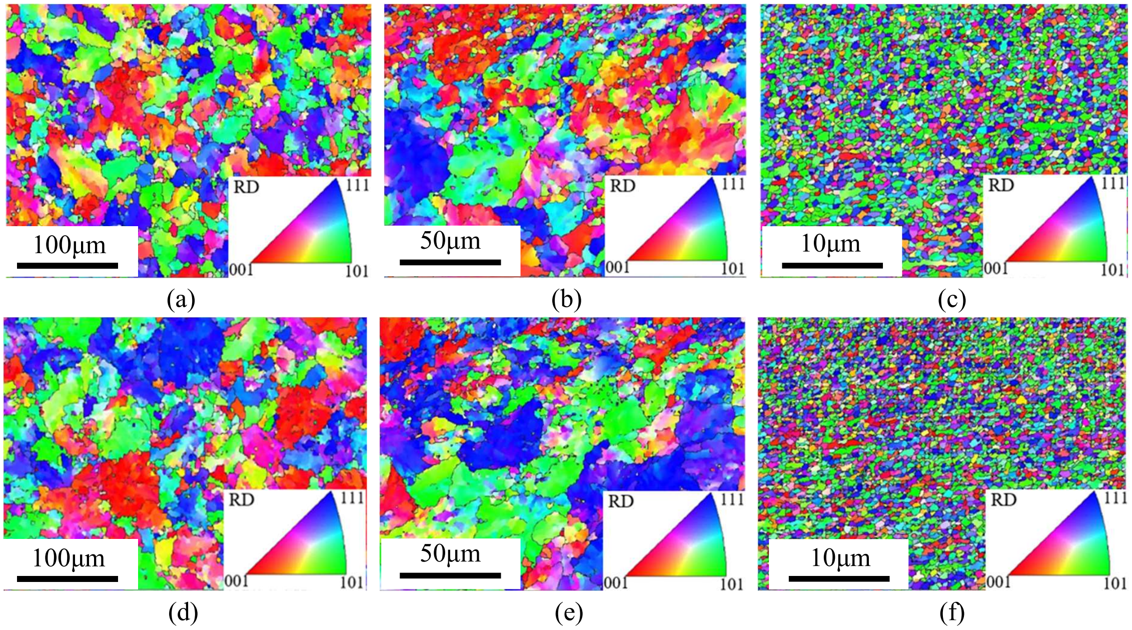

Fig. 6. IPFs of eutectoid and hypereutectoid rail in different zones, (a) eutectoid rail-matrix zone; (b) eutectoid rail-transition zone; (c) eutectoid-severely deformed zone; (d) hypereutectoid rail-matrix zone; (e) hypereutectoid rail-transition zone; (f) hypereutectoid rail-severely deformed zone.

Fig. 7 presents the grain boundary (GB) maps of eutectoid and hypereutectoid rail steels in different zones after testing. The GB map can describe the grain boundary angle and the grain size. Two types of grain boundaries can be observed: low angle grain boundaries (LAGBs) from 0^{o} to 15^{o} (green curves), and high angle grain boundaries (HAGBs) from 15^{o} to 65^{o} (black curves). With the increase in deformation (from the matrix zone to the transition zone and to the severely deformed zone), the size of grains decreases gradually (Fig. 7g). In the severely deformed zone, nano-grains with average diameters of 0.548 and 0.417 μm can be observed. Concerning the grain boundary angles, the content of HAGBs and LAGBs would experience two transitions (Fig. 7h). In the initial deformation stage (from the matrix zone to the transition zone) (Fig. 7a, b, d and e), the HAGBs would be transformed into LAGBs. Therefore, the defects of rail materials are dominated by the low angle sub-grain structure at the initial stage of deformation, which implies an increase in the lattice defects and the dislocation density. In the severely deformed zone (Fig. 7c and f), the LAGBs would be transformed into HAGBs, which indicates that the surface material would have undergone a dynamic recrystallization under cyclic loading [18].

The hypereutectoid rail has a higher content of LAGBs (52.98%) than eutectoid rail (41.78%) in the matrix zone (Fig. 7a and d). The more LAGBs in the matrix zone, the higher the dislocation density is, which could enhance the dislocation strengthening and increase the strength and hardness of the rail material. In the transition zone (Fig. 7b and e), the content of LAGBs of hypereutectoid rail (83.4%) is slightly larger than eutectoid steel (78.57%). This might be related to the fact that the dislocation tangling in hypereutectoid rail steel is more serious in the transition zone. In the severely deformed zone, the content of HAGBs of eutectoid and hypereutectoid rail steels are nearly the same (i.e., 91.45% and 90.6%).

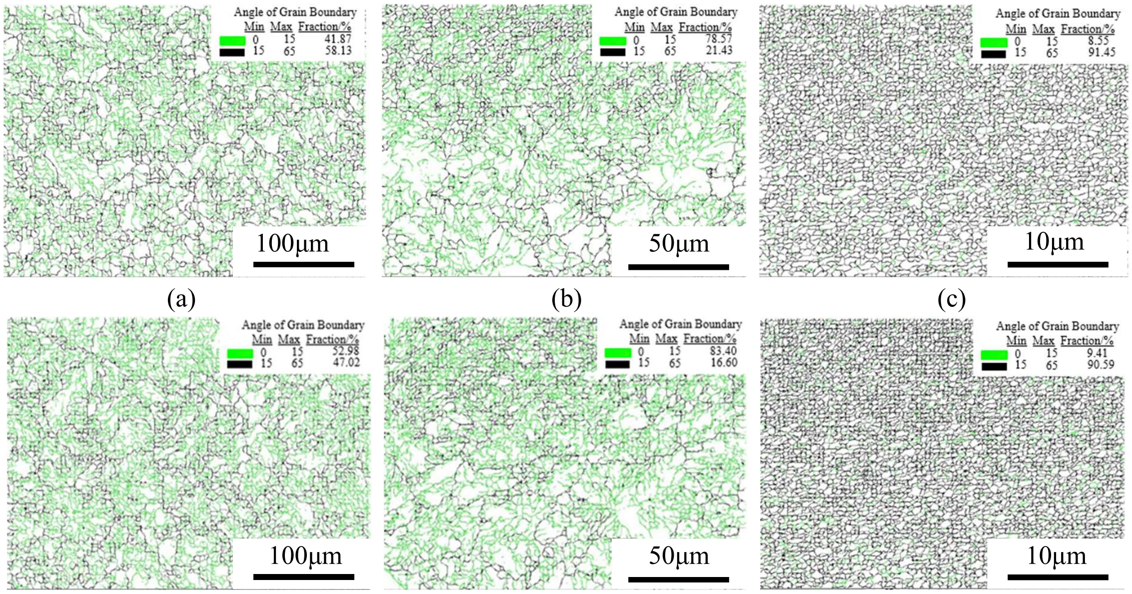

(a) (b) (c)

(d) (e) (f)

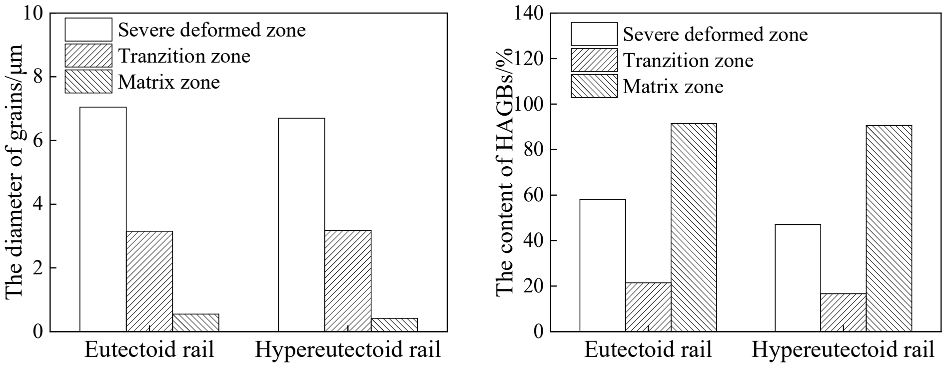

(g) (h)

Fig. 7. IPF and grain boundary map of hypereutectoid rail, (a) eutectoid rail-matrix zone; (b) eutectoid rail-transition zone; (c) eutectoid-severely deformed zone; (d) hypereutectoid rail-matrix zone; (e) hypereutectoid rail-transition zone; (f) hypereutectoid rail-severely deformed zone; (g) the average grain diameter and (h) the content of HAGBs of eutectoid and hypereutectoid rail steels.

Fig. 8 shows the pole figure (PF) of eutectoid and hypereutectoid rail steels after testing. The PF is the method used to determine whether a preferred orientation (i.e., texture) is formed after plastic deformation. The PFs of the three crystal planes {001}, {111} and {110} have been conducted in different zones. On the right is the scale of density intensity. The higher the density intensity, the more obvious the preferred orientation is in the deformed materials. It could be observed that for the eutectoid rail, with the increase in the deformation (from matrix zone to transition zone and to severely deformed zone), the maximum density intensity increases from 2.34 to 3.32 and to 3.82, respectively. In all three zones, the grains of eutectoid rail are distributed in a random orientation. Concerning the hypereutectoid rail, the maximum density intensities of the three different zones are 3.55, 4.38 and 3.54, respectively. Therefore, in the transition, the {110} plane along the RD direction of hypereutectoid rail has a more obvious preferred orientation than eutectoid rail.

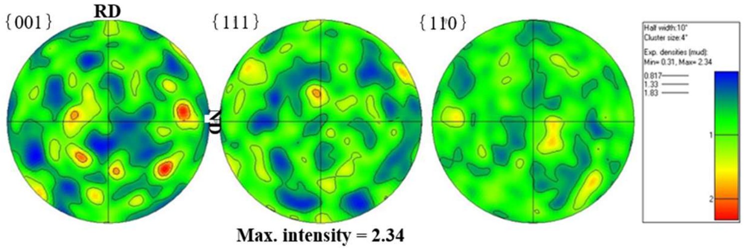

(a) eutectoid rail-matrix zone

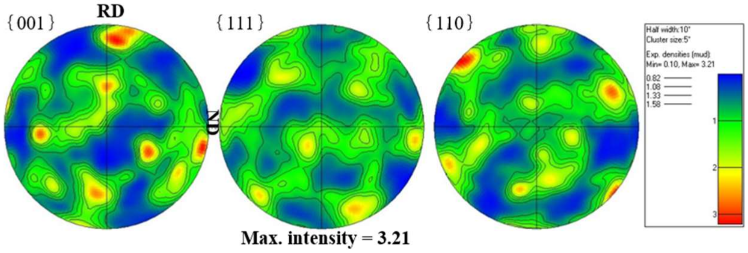

(b) eutectoid rail-transition zone

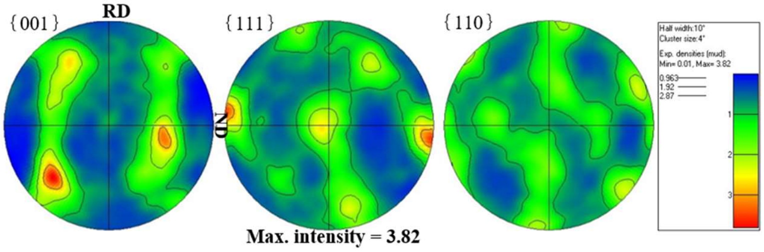

(c) eutectoid rail-severe deformed zone

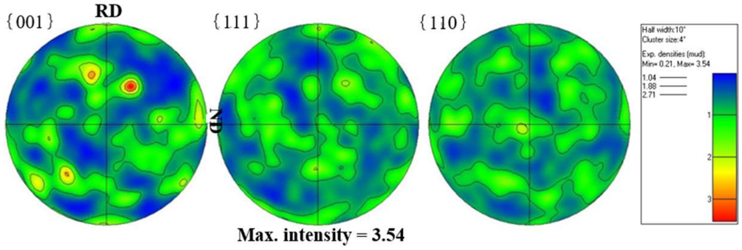

(d) hypereutectoid rail -matrix zone

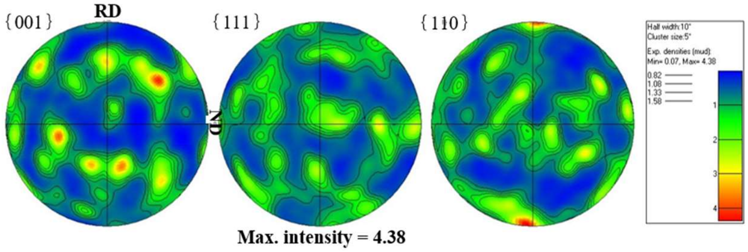

(e) hypereutectoid rail-transition zone

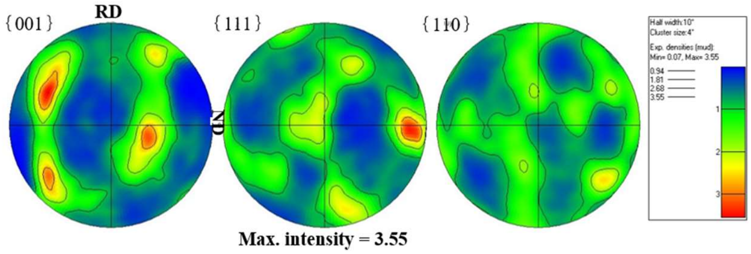

(f) hypereutectoid rail-severe deformed zone

Fig. 8. Pole Figures (PFs) in {001}, {111} and {110} crystal planes with an intensity legend, (a) eutectoid rail-matrix zone; (b) eutectoid rail-transition zone; (c) eutectoid-severely deformed zone; (d) hypereutectoid rail-matrix zone; (e) hypereutectoid rail-transition zone; (f) hypereutectoid rail-severely deformed zone.

During the deformation of grains, geometrical necessary dislocations (GNDs) are required to maintain the lattice continuity. Besides, the value of local misorientation (LM) could reflect the density of GNDs (ρ^{GND}). Fig. 9 shows the local misorientation (LM) of eutectoid and hypereutectoid rail steels in different zones. It could be observed that, in the initial deformation stage (from the matrix zone to the transition zone) the concentration range of the LM increases from 0~2° to 0~3° both for eutectoid and hypereutectoid rails (Fig. 9a, b, d and e). The low LM means that there are few dislocations in the matrix zone while the increase in LM indicates that numerous dislocations have initiated and piled-up during the initial stage of deformation. However, in the severely deformed zone (Fig. 9c and f), the LM of the rail decreases to the range of 0~1.5°, even smaller than that of the matrix. It is proved that, with the increase in the deformation, due to the dynamic recrystallization, the ρ^{GND} decreases as the dislocation contributes to the grain boundaries, which could result in the decrease in the LM.

Fig. 9g shows the average values of LM of eutectoid and hypereutectoid rails in different zones. The hypereutectoid rail in the matrix zone and the transition zone are larger than those of eutectoid rail. While, in the severely deformed zone, the average value of LM of eutectoid and hypereutectoid rails is nearly the same. This phenomenon indicates that more GNDs in hypereutectoid rail would contributed to the grain boundaries and hypereutectoid rail would experience more severe dynamic recrystallization than eutectoid rail.

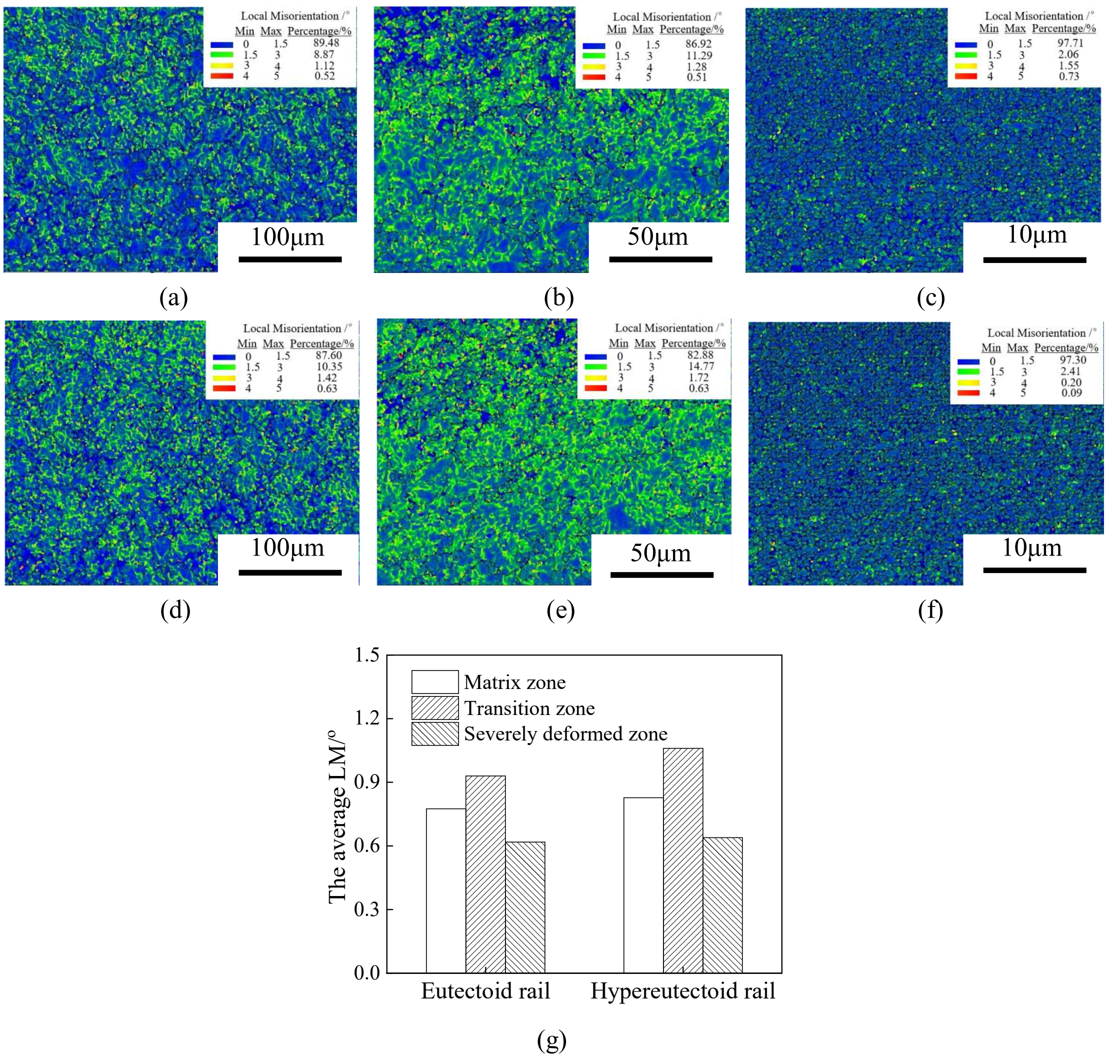

Fig. 9. Local misorientation (LM), (a) eutectoid rail-matrix zone; (b) eutectoid rail-transition zone; (c) eutectoid-severely deformed zone; (d) hypereutectoid rail-matrix zone; (e) hypereutectoid rail-transition zone; (f) hypereutectoid rail-severely deformed zone; (g) the average values of LM.

Fig. 10 shows the distribution of deformed structure, substructure and recrystallized grains of eutectoid and hypereutectoid rails in different zones. In the initial deformation stage (i.e., from the matrix zone to the transition zone) (Fig. 10a, b, d and e), the contents of the recrystallization structure and substructure decrease, while the content of the deformation structure increases. This is due to the fact that the material defects are dominated by the dislocation initiation and plastic deformation in the initial stage of deformation. In the severely deformed zone (Fig. 10c and f), the content of recrystallization structure and substructure of rail material increases significantly, while the content of deformation structure decreases sharply. It could be explained by the fact that dislocations on the surface material contribute to the grain boundary, leading to the dynamic recrystallization in the severely deformed zone. This result is consistent with the results from the GB maps and the LM of the rail materials (Fig. 7 and 9).

In the matrix zone, the content of the deformed grain and the recrystallized structure of the eutectoid and hypereutectoid rail steels are similar (Fig. 10a and d). However, in the severely deformed zone (Fig. 10c and f), the substructure of eutectoid rail (70.85%) is higher than that of hypereutectoid rail steel (52.99%) while the recrystallized proportion of eutectoid rail (14.52%) is lower than that of hypereutectoid rail (26.41%). Therefore, the hypereutectoid rail steel in the severely deformed zone has undergone a more severe recrystallization process than eutectoid rail.

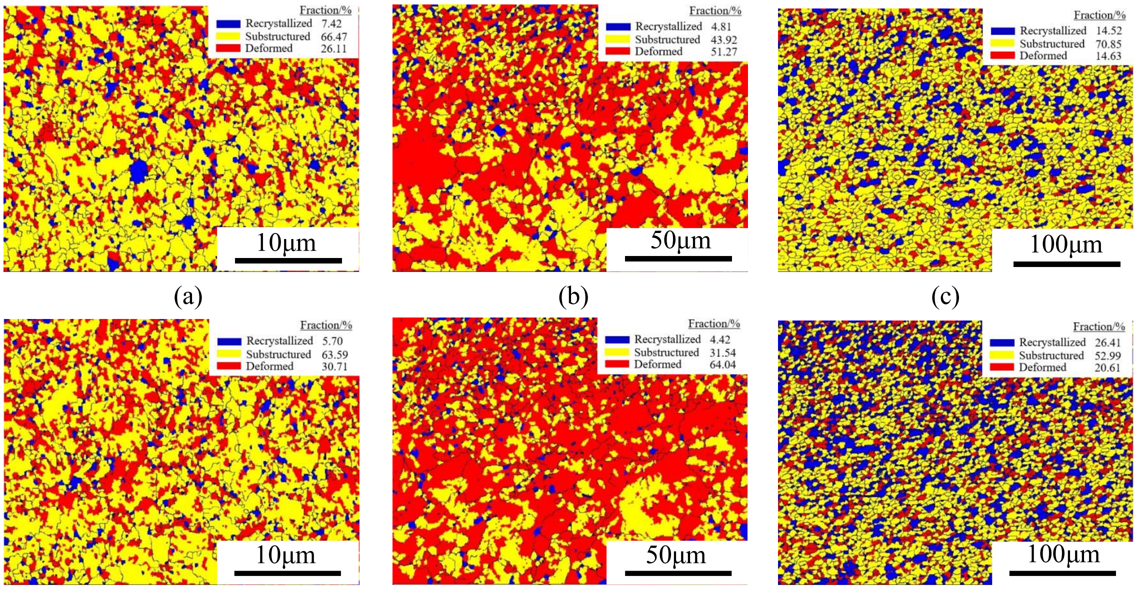

(a) (b) (c)

(d) (e) (f)

Fig. 10. The recrystallization, substructure and deformed structure of rail steels, (a) eutectoid rail-matrix zone; (b) eutectoid rail-transition zone; (c) eutectoid-severely deformed zone; (d) hypereutectoid rail-matrix zone; (e) hypereutectoid rail-transition zone; (f) hypereutectoid rail-severely deformed zone.

3.4 TEM observation

Fig. 11 shows the TEM observations of the microstructure morphologies and the selected area electron diffraction (SAED) spots of eutectoid and hypereutectoid rail steels after testing. It could be observed that in the transition zone (Fig. 10a), the structure of the material is non-uniform, and both the recrystallized sub-grain and the broken pearlite structure could be observed. This is due to the fact that the deformation of the pearlite is highly related to the arrangement of the pearlite lamellar. For the pearlite where the lamellar direction is consistent with the running direction, the structure is less damaged and the degree of recrystallization is weak. Where the lamellar direction is perpendicular or at a large angle to rolling direction, the structure is severely damaged and the degree of recrystallization is high. The SEAD spot reveals that the diffraction spots of both ferrite and cementite are evolving to a ring shape. In the severely deformed zone (Fig. 11b), the pearlite structure of eutectoid rail is severely broken and the cementite plates could nearly not be observed. Under high magnification, recrystallized grains could be observed. Besides, the pearlite grains are severely refined and the electron diffraction of the selected area shows a ring shape.

Fig. 11c and d show the TEM observation of the microstructure morphologies of the hypereutectoid rail steel in the transition zone and the severely deformed zone, respectively. Compared with the eutectoid rail steel, in the transition zone, at the same distance from the surface (50μm), the microstructure of the hypereutectoid rail steel is damage is more mild. At low magnification, a clear cementite plate structure could be observed. The lamellar pearlite is squeezed and distorted and micro-shear bands could be observed. Furthermore, the shear bands could shear the lamellar pearlite into a sub-grain structure [31]. In the severely deformed zone, the hypereutectoid rail steel has undergone a more severe grain refinement process than eutectoid rail. At high magnification, almost no independent recrystallized grain structure could be observed, and the SAED spot is ring-shaped. In summary, these two rail steels have experienced the formation of shear bands under the action of dislocations in the pearlite lamellar structure in the initial deformation stage (i.e., the transition zone), and then the formation of sub-grains. Finally, ultra-fine recrystallized grains could be observed on the subsurface materials as a result of dynamic recrystallization process. At the same depth from the surface, the grain refinement in the severely deformed zone of hypereutectoid rail is more severe, while in the transition zone, the structure damage of hypereutectoid steel is more mild than eutectoid rail.

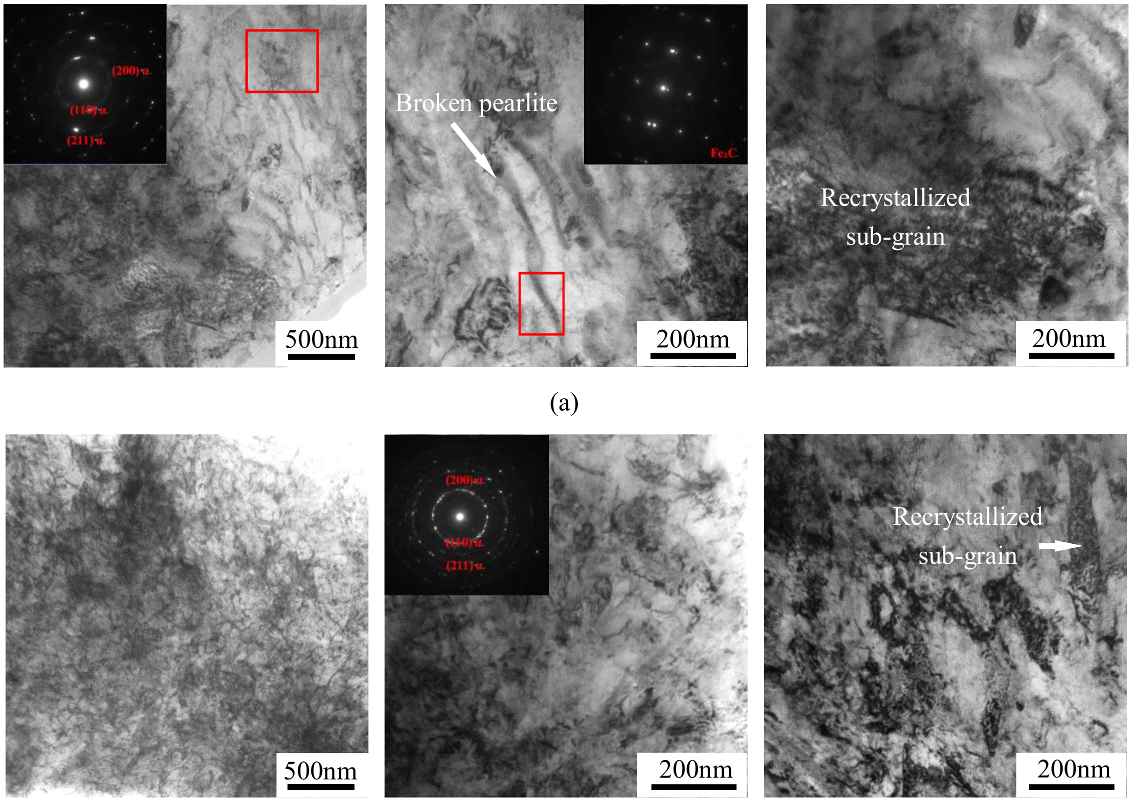

(a)

(b)

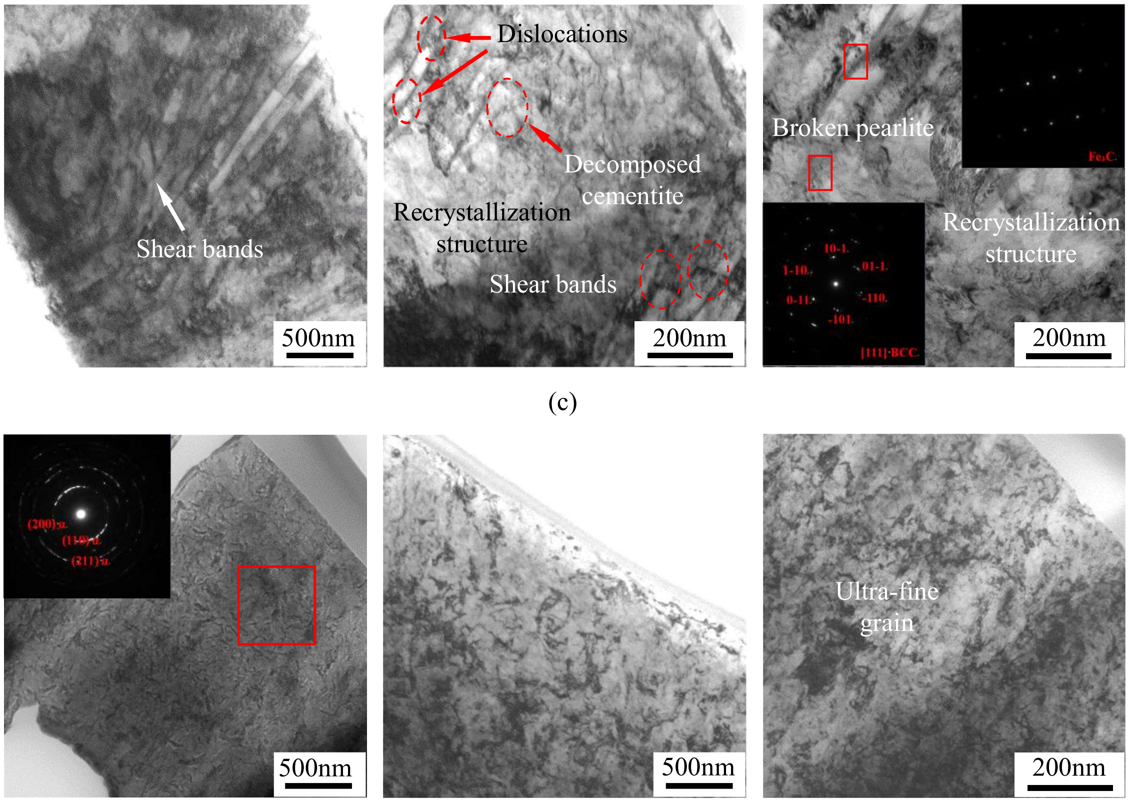

(c)

(d)

Fig. 11. TEM observation of microstructure deformation of rail, (a) eutectoid rail-transition zone; (b) eutectoid rail-severely deformed zone; (c) hypereutectoid rail-transition zone; (d) hypereutectoid rail-severely deformed zone.

3.5 The microstructure evolutions of rail steels

According to the observations and analysis above, the original equiaxed and undeformed coarse grains were transformed into nano-grains rich in HAGBs after rolling-sliding testing. The ultra-fine grains with HAGBs microstructure are consistent with the observations of microstructure on a field in-service rail [18]. The microstructure evolutions during rolling-sliding contact both of eutectoid and hypereutectoid rails were implemented by two mechanisms: the microstructure transition induced by the movement of dislocations and the following dynamic recrystallization. The initial microstructure deformation of pearlite and the breaking of cementite mainly occurred through the movement of dislocations, while the refinement of the grains and the formation the nanostructure grains mainly occurred through dynamic recrystallization.

During the initial deformation stage, the strain in the grains is relatively low and the initiation and movement of dislocations in ferrite plates dominated the microstructure evolution of the rail material. The ferrite had more slip systems and lower strength than cementite [23]. Therefore, the dislocations were preferentially initiated in ferrite plates. Furthermore, the pearlite grains orientated in anisotropy and the ferrite and cementite plates were aligned randomly to the shear stress. Where the lamellar direction was perpendicular to the shear stress, the dislocations slipped and piled-up at the interface between the ferrite and the cementite plates. The cementite would be curled and broken under a high density of dislocations (Fig. 10b and d). Where the lamellar direction was parallel to the shear stress, the dislocations slipped and piled-up at the grain boundaries. Two types of grain boundaries could be observed in rail materials: LAGBs and HAGBs. Basically, the LAGBs were considered as softer obstacles for dislocations, while HAGBs were harder obstacles [32]. With the elongation of durations, dislocations moved through the LAGBs while they piled-up at the HAGBs continually. The continuous accumulation of dislocations at the HAGBs adjusted the misorientation angles of adjacent grains and caused the transition from HAGBs to LAGBs (Fig. 6 and 9). Furthermore, pearlite grains rotated to the direction of shear stress gradually under the action of the high density of dislocations with shortened interlamellar spacing (Fig. 5a and c).

With the increase in the dislocation density, dense dislocation walls (DDWs) and dislocation tangles (DTs) were formed in the ferrite and segmented the pearlite into sub-grains. Besides, dislocations piled-up at the interfaces between pearlites and cementite plates which would lead to the strain localization and tear cementite to form the microshear bands (MSBs)

(Fig. 11b and d). Therefore, the dimensions of grains and the interlamellar spacing of pearlite decreased (Fig. 6).

With the further accumulation of deformation, the strain in the grains is relatively large and the dynamic recrystallization would dominate the microstructure evolution process of rail materials due to the severe plastic deformation, known as the continuous dynamic recrystallization (cDRX) [33]. The shear strain on the top of rail materials would accumulate as high as 12 to 14 [18] [19], which would high enough to cause a cDRX (e.g., ε>12). The cDRX originated form the transition of dislocations sub-boundaries into nanocrystallized grains with HAGBs. During this transition process, the LAGBs were converted into HAGBs (Fig. 6) and the grains were significantly refined into equiaxed nanocrystalline grains with a diameter less than 1 μm (Fig. 7b). Besides, a fibrous structure was formed (Fig. 5b and d).

3.6 Comparison of eutectoid and hypereutectoid rail steels

The hypereutectoid rail had finer interlamellar spacing and higher content of LAGBs (Fig. 7a) than eutectoid rail in the matrix zone. Therefore, the microstructure evolution of hypereutectoid was different from that of eutectoid rail after the rolling-sliding testing. In the initial deformation stage, the hypereutectoid rail would be deformed slightly and a texture could be observed. This is due to the higher content of LAGBs could coordinate the deformation of neighboring grains through rotating the pearlite orientation in the transition zone. In the severely deformed zone, the rail material would experience the cDRX process. As mentioned above, the cDRX was originated from the transition of dislocations sub-boundaries into nanocrystallized grains with HAGBs. In the present study, the hypereutectoid rail material had a higher content of LAGBs both in the transition zone and in the matrix zone. However, in the severely deformed zone, the HAGBs of eutectoid and hypereutectoid rail were nearly the same (Fig. 7a). This phenomenon indicated that the hypereutectoid rail would experience more severe LAGBs-to-HAGBs transitions and more severe cDRX than eutectoid rail in the severe deformed zone. The dynamic recrytallized grains could be the weak part for crack initiation and propagation [34]. Therefore, the hypereutectoid had a longer RCF crack length in the surface material. In summary, at the topmost layer, the hypereutectoid rail would present a higher cDRX degree in the severely deformed zone than eutectoid rail, which might be the possible reason for the lower RCF resistance of hypereutectoid rail in the present study.

4. Conclusions

In the present study, the wear and RCF performance and the subsurface microstructure evolution of eutectoid and hypereutectoid rail steels after testing were investigated systematically through SEM, EBSD and TEM. The pearlite grain deformation and refinement, the angle of grain boundaries and the recrystallization behaviour of these two rail materials after rolling-sliding tests were analyzed. The following conclusions could be obtained:

1. The hypereutectoid rail has a better resistance to wear, but a longer RCF crack length than eutectoid rail in the present study.

2. After the rolling-sliding testing, based on the plastic deformation and microstructure characteristics, the subsurface rail material could be divided into three zones: the severely deformed zone, the transition zone and the matrix zone. In the severely deformed zone, the original equiaxed and undeformed coarse grains in rail steels were transformed into nano-grains and most of the LAGBs were transformed into HAGBs.

3. The microstructure evolution during rolling-sliding contact both of eutectoid and hypereutectoid rails were implemented by two mechanisms. The initial microstructure deformation of pearlites and the breaking of cementite mainly occurred through the movement of dislocations while the following formation of the nanostructure grains mainly occurred through the cDRX.

4. The microstructure of hypereutectoid rail would deform more mildly in the transition zone, but would present a more severe cDRX process in the severely deformed zone than eutectoid rail.

Acknowledgments

The work was supported by National Natural Science Foundation of China (Nos. 51775455 and 52027807) and Sichuan Science and Technology Program (No. 2020ZDZX0011).

References

[1] D. Benoît, B. Salima, R. Marion, Multiscale characterization of head check initiation on rails under rolling contact fatigue: Mechanical and microstructure analysis, Wear 366-367 (2016) 383–391.

[2] A. Al-Juboori, D. Wexler, H. Li, H. Zhu, C. Lu, A. McCusker, J. McLeod, S. Pannil, Z. Wang, Squat formation and the occurrence of two distinct classes of white etching layer on the surface of rail steel, International Journal of Fatigue 104 (2017) 52–60.

[3] Z.F. Wen, X.S. Jin, X.B. Xiao, Z.R. Zhou, Effect of a scratch on curved rail on initiation and evolution of plastic deformation induced rail corrugation, International Journal of Solids

and Structures 45(7–8) (2008) 2077-2096.

[4] W.J. Wang, H.M. Guo, X. Du, J. Guo, Q.Y. Liu, M.H. Zhu, Investigation on the damage mechanism and prevention of heavy-haul railway rail, Engineering Failure Analysis 35 (2013) 206–218.

[5] J.J. Ding, R. Lewis, A. Beagles, J.P. Wang, Application of grinding to reduce rail side wear in straight track, Wear 402–403 (2018) 71–79.

[6] Q. Lai, R. Abrahams, W.Y. Yan, C. Qiu, P. Mutton, A. Paradowska, X.Y. Fang, M. Soodi, X.H. Wu, Effects of preheating and carbon dilution on material characteristics of laser-cladded hypereutectoid rail steels, Materials Science & Engineering: A 712 (2018) 548–563.

[7] K. Zhou, H.H. Ding, R.X. Wang, J.Y. Yang, J. Guo, Q.Y. Liu, W.J. Wang, Experimental investigation on material removal mechanism during rail grinding at different forward speeds, Tribology International 143 (2020) 106040.

[8] Y. Hu, L.C. Guo, M. Maiorino, J.P. Liu, H.H. Ding, R. Lewis, E. Meli, A. Rindi, Q.Y. Liu, W.J. Wang, Comparison of wear and rolling contact fatigue behaviours of bainitic and pearlitic rails under various rolling-sliding conditions, Wear 460–461 (2020) 203455.

[9] K. Mishra, A. Singh, Effect of interlamellar spacing on fracture toughness of nano-structured pearlite, Materials Science & Engineering: A 706 (2017) 22–26.

[10] X.C. Li, H.H. Ding, W.J. Wang, J. Guo, Q.Y. Liu, Z.R. Zhou, Investigation on the relationship between microstructure and wear characteristic of rail materials (2021) 107152.

[11] A.J. Perez-Unzueta, J.H. Beynon, Microstructure and wear resistance of pearlitic rail steels,

Wear 162–164 (1993) 173–182.

[12]S. Maya-Johnson, A.J. Ramirez, A. Toro, Fatigue crack growth rate of two pearlitic rail steels, Engineering Fracture Mechanics 138 (2015) 63–72.

[13]U. Masaharu, U. Kouichi, Application of hypereutectoid steel to heavy haul track rail, Processings of the TMS Fall Meeting, Thermomechanical processing and mechanical properties of hypereutectoid steels and cast irons. Warrendale (PA), USA, 1997.

[14]J. Takahashi, Y. Kobayashi, M. Ueda, T. Miyazaki, K. Kawakami, Nanoscale characterization of rolling contact wear surface of pearlitic steel, Journal Materials Science and Technology 29(2013) 1212–1218.

[15]J.F. Santa, P. Cuervo, P. Christoforou, M. Harmon, A. Beagles, A. Toro, R. Lewis, Twin disc assessment of wear regime transitions and rolling contact fatigue in R400HT–E8 pairs, Wear 432–433 (2019) 102916.

[16]M. Pletz, K.A. Meyer, D. Künstner, S. Scheriau, W. Daves, Cyclic plastic deformation of rails in rolling/sliding contact –quasistatic FE calculations using different plasticity models, Wear 436–437 (2019) 202992.

[17]M. Masoumi, A. Sinatora, H. Goldenstein, Role of microstructure and crystallographic orientation in fatigue crack failure analysis of a heavy haul railway rail, Engineering Failure Analysis 96 (2019) 320–329.

[18]F.A.M. Alwahdi, A. Kapoor, F.J. Franklin, Subsurface microstructural analysis and mechanical properties of pearlitic rail steels in service, Wear 302 (1–2) (2013) 1453–1460.

[19] G. Trummer, C. Marte, P. Dietmaier, C. Sommitsch, K. Six, Modeling surface rolling contact fatigue crack initiation taking severe plastic shear deformation into account, Wear 352-353 (2016) 136–145.

[20] J. Wen, J. Marteau, S. Bouvier, M. Risbet, F. Cristofari, P. Secordel, Comparison of microstructure changes induced in two pearlitic rail steels subjected to a full-scale wheel/rail contact rig test, Wear 456–457 (2020) 203354.

[21] A. Kumar, G. Agarwal, R. Petrov, S. Goto, J. Sietsma, M. Herbig, Microstructural evolution of white and brown etching layers in pearlitic rail steels, Acta Materialia 171 (2019) 48–64.

[22] H. Chen, Y.Z. Ji, C. Zhang, W.B. Liu, H. Chen, Z.G. Yang, L.Q. Chen, C.L. Chen, Understanding cementite dissolution in pearlitic steels subjected to rolling-sliding contact loading: A combined experimental and theoretical study, Acta Materialia 141 (2017) 193–205.

[23] T. Teshima, M. Kosaka, K. Ushioda, N. Koga, N. Nakada, Local cementite cracking induced by heterogeneous plastic deformation in lamellar pearlite, Materials Science & Engineering: A 679 (2017) 223–229.

[24] Y.J. Li, P. Choi, C. Borchers, S. Westerkamp, S. Goto, D. Raabe, R. Kirchheim, Atomic-scale mechanisms of deformation-induced cementite decomposition in pearlite, Acta Materialia 59 (2011) 3965–3977.

[25] F. Wetscher, A. Vorhauer, R. Stock, R. Pippan, Structural refinement of low alloyed steels during severe plastic deformation, Materials Science & Engineering: A 387 (2004) 809–816.

[26] W.J. Nam, C.M. Bae, S.L. Oh, S.J. Kwon, Effect of interlamellar spacing on cementite

dissolution during wire drawing of pearlitic steel wires, Scripta Materialia 42(5) (2000) 457–463.

[27] A. Mazzù, G. Donzella, A model for predicting plastic strain and surface cracks at steady-state wear and ratcheting regime, Wear 400–401 (2018) 127–136.

[28] N.P. Suh. The delamination theory of wear. Wear 25(1) (1973) 111–124.

[29] X. Hu, P. Van Houtte, M. Liebeherr, A. Walentek, M. Seefeldt, H. Vandekinderen, Modeling work hardening of pearlitic steels by phenomenological and Taylor-type micromechanical models. Acta Materialia 54 (2006) 1029–1040.

[30] C.G. He, H.H. Ding, L.B. Shi, J. Guo, E. Meli, Q.Y. Liu, A. Rindi, Z.R. Zhou, W.J. Wang, On the microstructure evolution and nanocrystalline formation of pearlitic wheel material in a rolling-sliding contact, Materials Characterization 164 (2020) 110333.

[31] Y. Hu, L. Zhou, H.H. Ding, R. Lewis, Q.Y. Liu, J. Guo, W.J. Wang, Microstructure evolution of railway pearlitic wheel steels under rolling-sliding contact loading, Tribology International 154 (2021) 106685.

[32] L. Fourel, J. Noyel, E. Bossy, X. Kleber, P. Sainsot, Fabrice Ville, Towards a grain-scale modeling of crack initiation in rolling contact fatigue- Part 2: Persistent slip band modeling, Tribology International 163 (2021) 107173.

[33] T. Sakai, A. Belyakov, R. Kaibyshev, H. Miura, J.J. Jonas, Dynamic and post-dynamic recrystallization under hot, cold and severe plastic deformation conditions, Progress in Materials Science 60 (2014) 130–207.

[34] Y.H. He, X.Q. Hou, C.H. Tao, F.K. Han, Recrystallization and fatigue fracture of single crystal turbine blades, Engineering Failure Analysis 18(3) 2011 944–949.